



On the microstructure and tensile behaviour of nanostructured NiTi alloy produced by electroplastic rolling

J. V. Tilak Kumar¹, S. Jayaprakasam^{†,1}, V. S. Senthil Kumar¹, K. A. Padmanabhan¹,
A. Frolova², V. Stolyarov³

[†]sudhajayaprakash@gmail.com

¹Department of Mechanical Engineering, College of Engineering, Guindy, Anna University, Chennai, 600025, India

²Advanced Forming Research Centre, University of Strathclyde, Renfrewshire, PA4 9LJ, UK

³Mechanical Engineering Research Institute, RAS, Moscow, 101990, Russia

Electroplastic rolling was employed to produce nanostructured (NS), near-equiatomic NiTi alloy from a coarse grained NiTi nugget (ingot), which was produced using vacuum induction melting, followed by quenching in water from a temperature of 800°C. The microstructure of NS NiTi was characterized using X-ray Diffraction (XRD) and transmission electron microscopy (TEM). XRD analysis revealed that the NS NiTi is predominantly martensitic at room temperature, with less than $\approx 10\%$ of the austenite phase. The NS NiTi alloy has an average grain size of ≈ 36 nm. TEM investigation confirmed the presence of grains that are less than 10 nm in size and no amorphous zones were detected. The NS martensitic NiTi alloy specimens were tested in tension at two different strain rates (10^{-2} and 10^{-1} s⁻¹). In contrast to a stress-strain profile expected in a martensitic NiTi alloy, the stress-strain curves show conventional tensile behaviour. The observed UTS was high, around ≈ 1800 MPa, with a less than usual elongation to failure of $\approx 6\%$. The presence of dimples on the fracture surfaces can be seen in scanning electron microscopy (SEM) images, which is indicative of ductile fracture. The role of grain size in the observed deformation and fracture features is also discussed.

Keywords: nanostructured NiTi, martensitic NiTi, shape memory alloy (SMA), tensile behaviour.

1. Introduction

NiTi is an extensively researched alloy, which is used in a number of critical applications owing to its unique properties, namely, shape memory effect and superelasticity [1]. Martensitic transformation is the phenomenon responsible for both superelasticity and shape memory effect observed in NiTi alloys. This reversible diffusionless transformation takes place when the temperature or stress states are varied appropriately, resulting in a change in the crystal structure involving coordinated short relative movement of atoms not exceeding the span of one lattice spacing. In NiTi, this solid to solid transformation involves the phases austenite and martensite, the former is stable at high temperatures and has a CsCl B2 crystal structure and is considered as the parent phase, while the latter is stable at low temperatures and has a monoclinic B19' crystal structure [2]. NiTi is classified as a smart material, which constitutes a part of an important class of alloys, but is yet to be studied fully [3]. This alloy has diverse applications such as SMA (shape memory alloy) tires for rovers, vibration dampers for space-borne cryo-coolers, mechanical actuators, intravascular stents, fixtures for bone fracture, orthodontic wires, etc. [4–9]. In all these applications, strict control over the mechanical response of NiTi alloy is required. Apart from its microstructure, the mechanical behaviour of NiTi is highly influenced by loading conditions like stress, temperature and loading

rate [10–12]. As is well known, microstructure-mechanical response correlation is essential for a better understanding of the in-service performance of any material. Besides, it is important not only to increase the mechanical properties of SMA alloys, but also not to worsen, or even improve, the functional properties — superelastic recovery strain and the shape memory effect on bending [13]. As shown in [14], the improvement in functional properties was associated with a decrease in grain size and the need to create nanostructures in SMA alloys arises. To do this, it was necessary to apply large deformations with a true strain >1 , which was successfully demonstrated using some severe plastic deformation (SPD) techniques, namely high pressure torsion (HPT) for thin disks of small diameter (less than 10 mm) and equal channel angular pressing (ECAP) for workpieces with a diameter of more than 10 mm.

It was shown that very high strengths of around 2600 MPa can be achieved by a nanostructured NiTi produced by severe plastic deformation [15]. The nanostructured NiTi produced by various severe plastic deformation techniques has many advantages such as increased strength, superior fatigue performance, corrosion resistance, etc., and behaves differently compared with NiTi of the same composition, but of a coarse-grained microstructure [16–20]. In particular, in medical applications, corrosion resistance is critical as Ni release from NiTi implants are known to cause toxicity and several undesired reactions in humans [21,22]. Producing

a nano-structured NiTi alloy in commercial quantities is challenging and nanostructure often has to be obtained in long parts with a thin section (strip or wire with a cross-section of 1–3 mm²), which cannot be done by traditional severe plastic deformation methods, hence new SPD techniques have been developed, with each having its own limitations [14,23,24]. From among the few viable SPD methods, Electroplastic Rolling (EPR) was employed in this study to successfully overcome the tendency of NiTi to become brittle during cold rolling [25]. In a series of studies carried out in the early 1970s, Russian researchers established that dislocations interact with electrons when current pulses are applied to a material during the deformation process [26]. It was demonstrated that the flow stress of several metals decreased during tensile deformation when current pulses are applied [26]. Since then, numerous experiments on some alloys have shown that the application of current pulses enhances the plasticity. The EPR process involves the application of the current pulses via a set of rollers used for deforming the material. The setup is very similar to that of a cold rolling process with the only key difference being the addition of provisions for supplying electrical current via the rollers. This method makes it possible to not only obtain a nanostructure but also to dramatically reduce the deforming forces and to remove the limitation of maximum deformation degree by means of high current density without significant heating, which is so necessary for structure refinement. One of the discussed mechanisms of electroplasticity, in addition to the possible thermal effect of the current, is the interaction of conduction electrons with defects that arise during plastic deformation, for example, dislocations [27]. For some alloys based on titanium and aluminium, it has been shown that the contribution of the electroplastic effect can be noticeably larger than the thermal Joule-Lenz effect [28]. It is especially important since this method can be applied to long thin semi-finished parts. A study on the effect of EPR on the deformability of NiTi revealed that high true strains in the range 1–1.8 can be effectively achieved without any macro defects by the application of sufficiently high current densities [29]. Furthermore, the application of very high current densities, around 300 A/mm², resulted in substantial heating of the work material, enough to cause recrystallization, according to the same study. These findings reiterate the need to identify ideal processing conditions by assessing the mechanical behaviour of the processed material. The main aim of this study is to assess the behaviour of the EPR processed NiTi alloy in the nano-structured state using tensile tests and correlate the results with the microstructure.

2. Experimental procedure

Near-equiatomic Ni_{50.7}Ti_{49.3} with a coarse grained (CG) structure was produced using vacuum induction melting, followed by water quenching from 800°C. The microstructure of the CG NiTi comprised mostly of equiaxed grains and the average grain size was ≈35 μm. (A detailed study on the microstructure and mechanical behaviour of this material can be found in [30]). The CG NiTi alloy was subjected to EPR and the process parameters are listed in Table 1. A schematic diagram and some additional details on the EPR

setup can also be found in [30]. A current pulse frequency of 1000 Hz with a sufficiently high current density was chosen as it is known to have a positive impact on deformability [31]. Multiple passes of EPR were carried out to reduce the thickness of the workpiece from 6.2 to 1.5 mm, resulting in a true strain of 1.42, which gave rise to NS NiTi. By water cooling the samples intermittently, the temperature was kept under control because EPR can significantly raise the temperature of the work-piece. XRD analysis was used to determine the phase distribution in the NS NiTi at room temperature. XRD Samples were manually polished under a continuous flow of water to keep the temperature rise and induced stress minimal to avoid phase transformation in the surface grains. Microstructure analysis was done using a 200 kV FEI Tecnai TEM and the fracture surfaces were examined using a Hitachi S-3400 N SEM. Uniaxial tensile tests at room temperature were carried out on an Instron testing machine at 10⁻² and 10⁻¹ s⁻¹. Miniature tensile specimens with the gauge section measuring 18 × 4 × 1.5 mm³ were used for the tensile tests.

Table 1. Process parameters of EPR.

Parameter	Value
Roll diameter	120 mm
Roll speed	60 mm s ⁻¹
Current pulse frequency	1000 Hz
Current pulse duration	1 × 10 ⁻⁴ s
Current density	80 A · mm ⁻²
ON/OFF time ratio	10
Reduction per pass	100 μm
True strain	1.42

3. Results and Discussion

3.1. XRD analysis

XRD analysis (Fig. 1a) of the NS NiTi reveals that the material is almost completely martensitic at room temperature. Residual austenite phase content was less than ≈10%. Data from peak fitting after deconvolution was used in the XRD calculations. It can be seen in Fig. 1a that the diffraction pattern contains 6 peaks which include a low-intensity peak belonging to the B2 (BCC crystal structure) austenite phase. As can be observed, the (011) reflection of the B2 austenite phase has the maximum peak broadening and consequently the highest value of FWHM (full width at half maximum) among all the peaks, indicating the presence of more defects and possibly a larger micro-strain in comparison with the B19' (monoclinic crystal structure) martensite phase. The domain size (approximate grain size) was calculated using the modified Scherrer equation (along with the least-squares method) (Eq. 1) [32], which yielded a value of ≈22 nm.

$$\ln(\beta) = \ln \frac{1}{\cos \theta} + \ln \frac{K\lambda}{D}, \quad (1)$$

where D — grain size, K — Scherrer constant, λ — wavelength of the X-ray (0.15406 nm), β — full width at half maximum, θ — peak position [32].

In principle, the Williamson-Hall method [33] can be used to know the micro-strain and the domain size (to compare the latter value with that obtained using the modified Scherrer equation) of the NS NiTi. However, the Williamson-Hall plot (Fig. 1b) in the present case showed a negative slope and so this method could not be used. This finding, however, is not unexpected because it has been reported that Williamson-Hall plots often show negative slopes when the domain size is below about 20 nm [34–37].

3.2. Microstructure of the NS NiTi

TEM image of NS NiTi (Fig. 2a) reveals the presence of heterogeneous microstructural features typical of metallic alloys processed by SPD. Very fine grains of size ranging between ≈ 5 and ≈ 30 nm are seen along with a few larger grains of size between 60 and 130 nm. The shapes of grains vary significantly from equiaxed to polyhedral forms. The average grain size was ≈ 36 nm, which is greater than the value obtained through XRD (≈ 22 nm). The average size of the polyhedral grains was ≈ 47 nm. Equiaxed grains appear to be smaller when compared with polyhedral grains. The presence of nano-grains is also confirmed by the SAED

pattern presented in Fig. 2b, which shows diffused rings belonging to different planes of the martensite and austenite phases. It is observed that some reflections were not detected in the TEM SAED pattern (Fig. 2b) compared with the XRD pattern (Fig. 1a) and vice-versa, which is attributed to the fact that the sampling area is extremely small in the TEM analysis. No precipitates were detected in both the XRD and TEM analyses. Careful examination of the microstructure (Fig. 2a) revealed that most regions comprise twinned martensite. Some of these regions are marked with red arrows. Based on the SAED analysis (Fig. 2b), it is clear that these regions belong to the B19' martensite phase. The size of the martensite grains observed varied between ≈ 60 and 150 nm. Though a few martensite grains appear to have sizes ranging between 30 and 50 nm in Fig. 2a, this could not be confirmed as the grain boundaries appear poorly defined due to the constraint in the resolution of the TEM image. The XRD peak corresponding to the B2 austenite phase (Fig. 1a) clearly appears broadened implying that this phase has a very high defect density and that the size of the grains belonging to this phase certainly falls in the nanocrystalline range. This B2 austenite peak most likely represents grains in the sub 50 nm range that formed at some levels of plastic

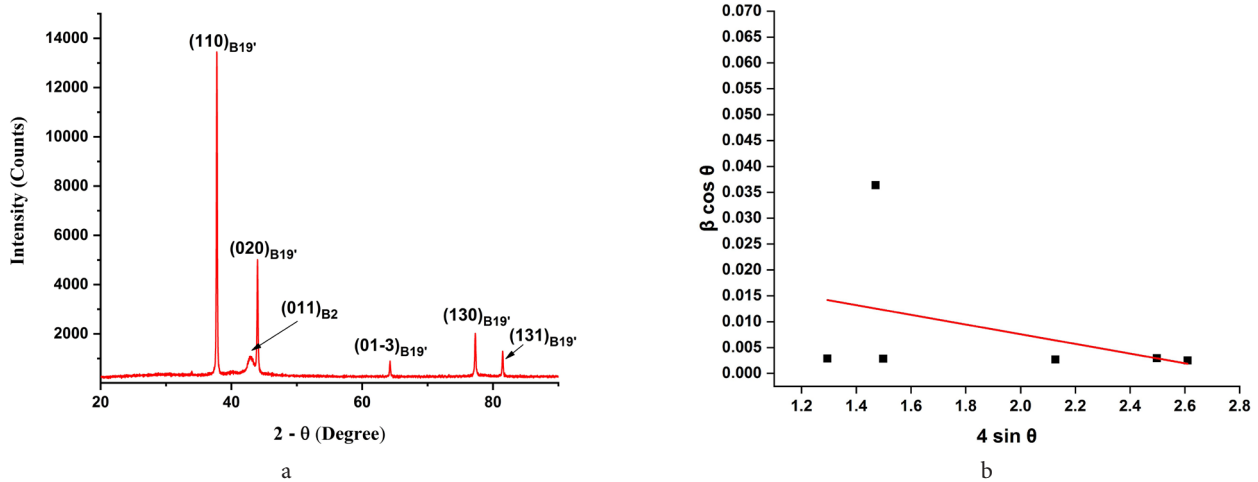


Fig. 1. XRD pattern of NS NiTi (B19' — martensite; B2 — austenite) (a) and corresponding Williamson-Hall plot (b).

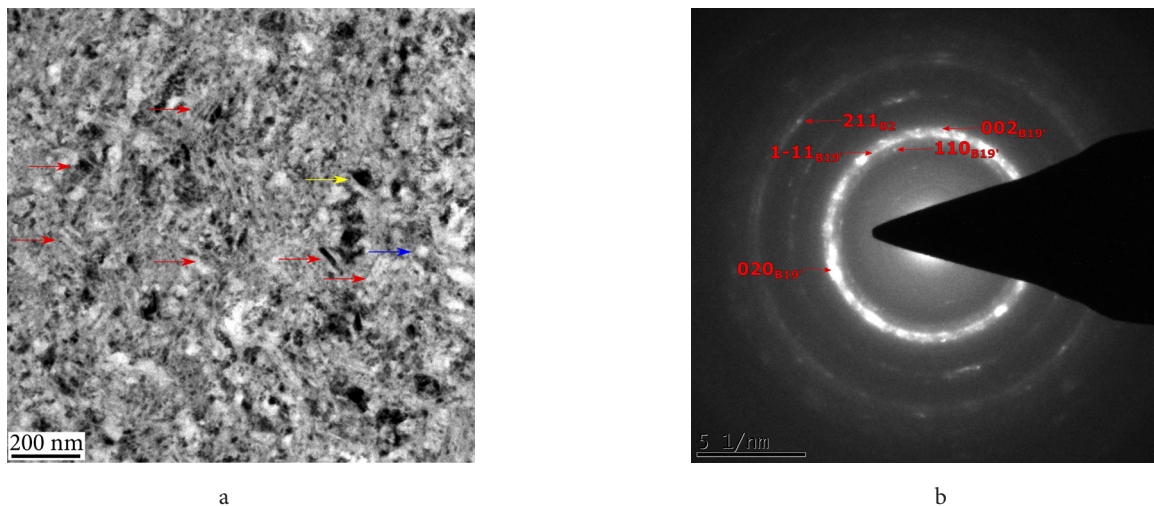


Fig. 2. (Color online) TEM microstructure of NS NiTi (equiaxed and polyhedral grains are marked with blue, and yellow arrows respectively; regions showing twinning are marked with red arrows) (a) and corresponding SAED pattern (b).

straining during the EPR process. It is to be noted that the NiTi in the coarse-grained state before EPR processing contained approximately 90% B2 austenite phase at room temperature, most of which transformed to B19' martensite phase post the EPR process. It can be hypothesized that during the EPR process stress-induced martensite transformation must have taken place due to the application of stresses, resulting in the formation of martensite. Some of these newly formed martensite could have transformed back to austenite as a consequence of the temperature rise due to adiabatic heating during the EPR process, resulting in a thermally induced reverse transformation. These forward and reverse transformations could have happened several times during the EPR passes though the extent of reverse transformation must be less as the samples were water-cooled between the passes. The application of high plastic strains usually results in an increase in the number of defects, which eventually refine the microstructure. The nanometre-sized martensite grains observed in the TEM image (Fig. 2a) could have formed directly because of stress-induced martensitic transformation of nanometre-sized austenite grains that were formed as a result of EPR and some of them may have formed from the refinement of larger martensite grains formed during the initial stages of deformation [38, 39]. Furthermore, the EPR process could have changed the transformation temperatures in such a way that the final material is martensitic at ambient temperature.

Narrow zones of intense shear strain were observed in some regions together with twinned martensite in the TEM images, which are indicative of localized, very severe plastic deformation. These regions are also seen in both the TEM bright and dark field images — please see Fig. 3a,b,c and d. These nano-bands contain very fine nano-grains that appear deformed and are revealed predominantly in the TEM dark field image, Fig. 3d. The average width of these shear bands was ≈ 40 nm and they are 2 to 5 grains across in their width. The length of these bands ranged from 50 to 140 nm. These regions also exhibit high dislocation densities. A few twinned martensite grains with sizes in the 30 to 50 nm range can be seen in the dark field image shown in Fig. 3b. As in Fig. 2a, the grain boundaries are poorly defined in Fig. 3b, but the quality of the image appears to be slightly better. A few large polyhedral grains could also be seen in the TEM dark field image, Fig. 3d. Some of these contain the B19' martensite phase and can be identified by their twinned structure. The large polyhedral grains belonging to the B2 austenite phase could have formed as a result of localized, heterogeneous dynamic recrystallization initiated by a rise in temperature during EPR as the samples were water-cooled only between the passes and not during entire processing. These polyhedral grains are observed mostly near the banded regions as they are one of the preferred sites for nucleation [40]. Though the fraction of these shear bands could not be quantitatively estimated in this case owing to the small TEM sample area, the shear bands do

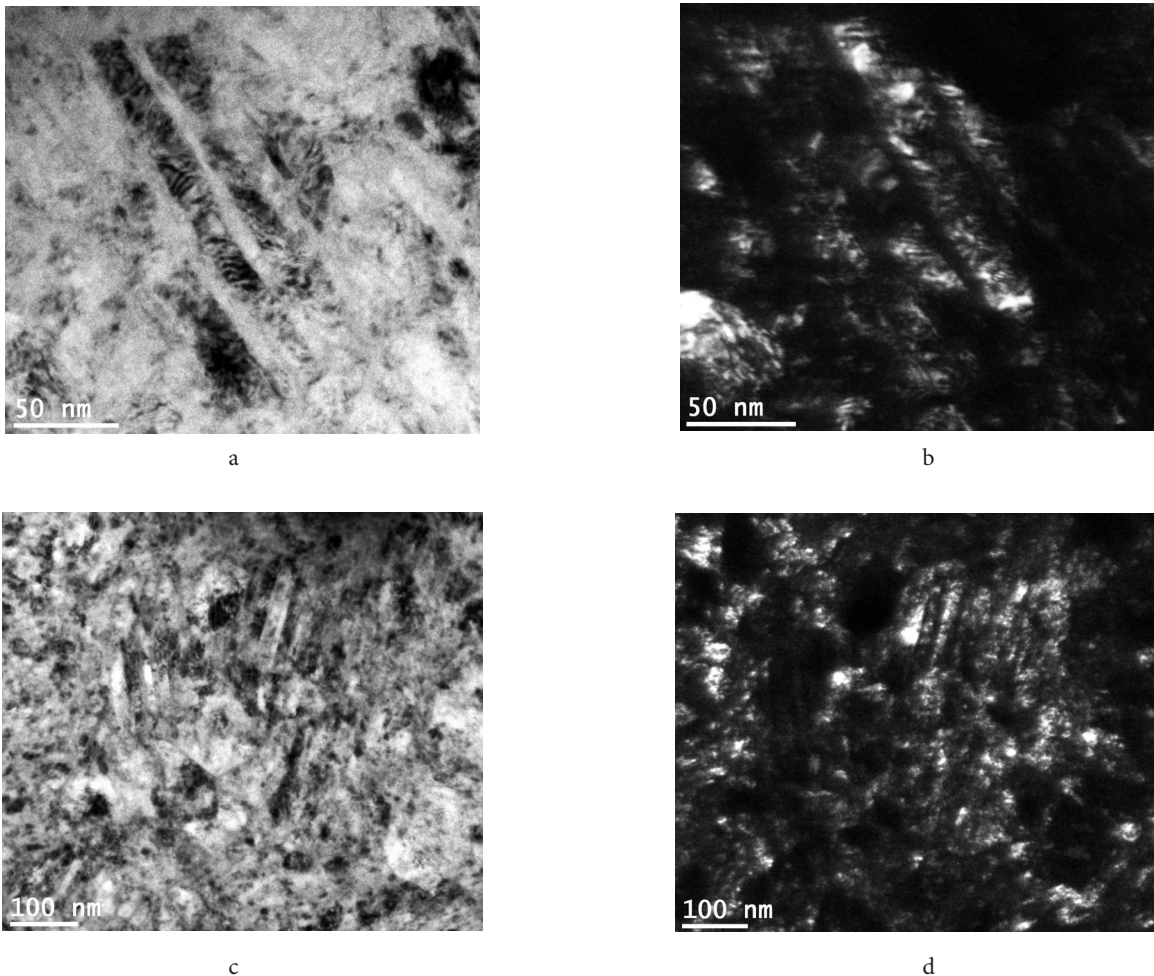


Fig. 3. TEM images of NS NiTi in bright field pictures (a) and (c); and in dark field (b) and (d).

appear similar to those seen in the TEM pictures presented by other workers [12,41]. The presence of these shear bands in large numbers suggests that the material could fail prematurely by their propagation on further application of strain.

3.3. Tensile behaviour

Uniaxial tensile tests were carried out at room temperature (25°C) at two different (initial) strain rates in the quasi-static regime (10^{-2} and 10^{-1} s $^{-1}$). From Fig. 4 it is seen that the yield strength increases slightly with strain rate. Elongation to failure is unusually low and is almost the same for both the tests, with the highest value being $\approx 6\%$ for the test done at 10^{-2} s $^{-1}$. The highest UTS value of 1865 MPa was observed in the test done at 10^{-1} s $^{-1}$. The linear stress-strain range observed in both tests was high ($\approx 2\%$). A strain gauge could not be used due to the small size of the specimens, which does not allow a high degree of confidence being placed on the magnitude measured.

From the XRD data, it is evident that the NS NiTi is almost fully martensitic at room temperature. The stress-strain curves in Fig. 4 did not exhibit plateauing, which is typical of martensitic shape memory NiTi alloy deformed in tension. Instead, it exhibits normal tensile behaviour. When NiTi with a B19' microstructure is subjected to tension at quasi-static loading rates, it generally undergoes detwinning, which manifests as a stress plateau in the stress-strain curve [42]. The lack of a stress plateau indicates that the NS NiTi underwent only a negligible amount of detwinning, the extent of which is

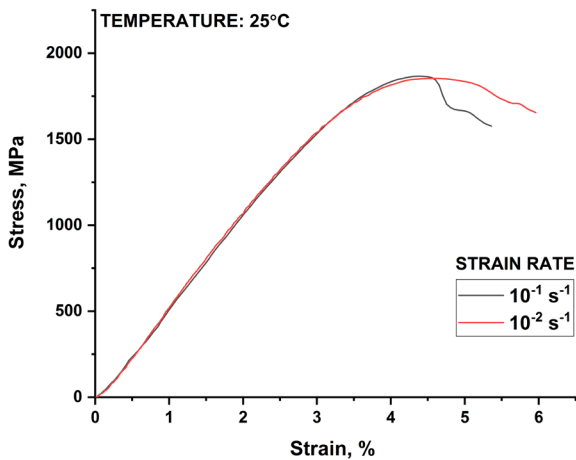


Fig. 4. (Color online) Stress-strain curves for the NS NiTi tested at different strain rates.

directly connected to the shape recovery. Detwinning, seen as a stress plateau during tensile deformation of martensitic NiTi, is known as a reliable indicator of good shape recovery [43]. Some of the twinned martensite grains may have undergone detwinning, but the net outcome suggests that this process was affected by the presence of other entities. Perhaps even the size of the twinned martensite grains could have played a significant role here. A stress plateau is also typically observed in a material undergoing stress-induced martensitic transformation. Even if the small fraction of austenite grains existing in the original microstructure underwent stress-induced martensite transformation during tensile deformation, the amount of austenite present in the EPR treated sample was too little to show a macroscopic effect. Therefore, at the present level of accuracy, the role of the $\approx 10\%$ volume fraction of austenite on the tensile deformation appears to be negligible, which is dominated by the nanometre scale grain size and the number of shear bands present right from the beginning of tensile deformation. The net result is a flow curve characteristic of dislocation slip deformation followed by a premature fracture facilitated by the presence of shear bands and high defect density [44]. In addition, the above statements are consistent with the known fact that when the defect density increases beyond a point the shape memory effect begins to decline [45].

3.4. Fracture analysis

The fracture surfaces of the NS NiTi tensile tested samples at different strain rates showed practically no difference. These surfaces revealed the presence of dimples, characteristic of ductile fracture — see, for example, Fig. 5 a and b. The patterns observed in both the fracture surfaces are similar. The only difference lies in the mean size of the dimples — 6 and 7 μm respectively (extremely close) for strain rates of 10^{-2} and 10^{-1} s $^{-1}$, consistent with the similar ductility exhibited by the material at the two strain rates. These results also suggest that the final failure is a result of cavity coalescence.

4. Conclusions

EPR processed Ni_{50.7}Ti_{49.3}, which has undergone a true strain of 1.42, possesses a martensitic microstructure at room temperature, of average grain size of 36 nm. A high UTS of 1865 MPa was observed in a tensile test carried out at 10^{-1} s $^{-1}$, with an elongation to failure only of $\approx 5.5\%$. A stress plateau typically observed in the tensile stress-strain

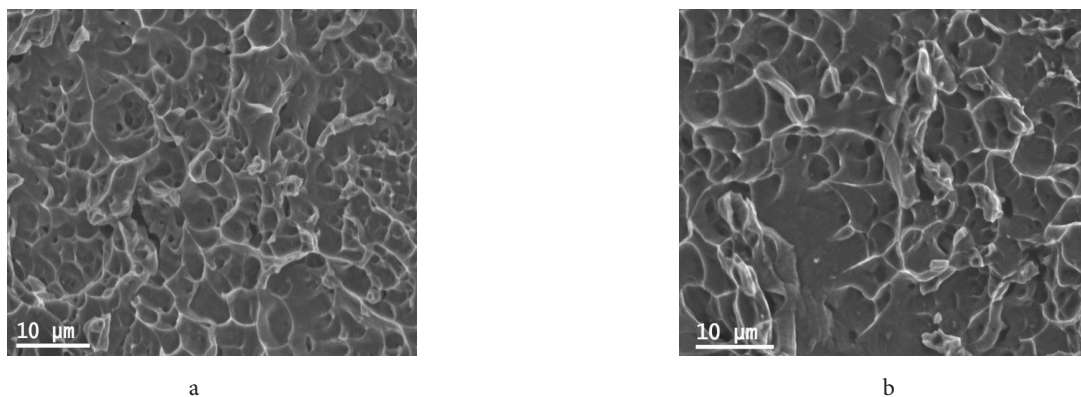


Fig. 5. SEM fracture surfaces of NiTi tested at 10^{-2} s $^{-1}$ (a) and 10^{-1} s $^{-1}$ (b).

curve of a martensitic NiTi alloy was not seen, implying that the detwinning process was impeded. For this reason, this material is expected to possess poor shape recovery, although this cannot be asserted with certainty by tensile tests alone. This behaviour is traced to the nanoscale grain size and the presence of numerous, localized deformation zones in the starting material itself. It is understandable that such a microstructure has very limited ductility.

Acknowledgements. This work was supported by Department of Science and Technology, Government of India [No. DST/INT/RFBR/IDIR/P-04/2016] and RFBR [Grant No. 16-58-48001] of Russia.

References

- W.J. Buehler, F.E. Wang. Ocean Eng. 1, 105 (1968). [Crossref](#)
- K. Otsuka, T. Kakeshita. MRS Bull. 27. 91 (2002). [Crossref](#)
- A.N. Bucsek, H.M. Paranjape, A.P. Stebner. Shap. Mem. Superelasticity. 2, 264 (2016). [Crossref](#)
- S.A. Padula, J. Benzing, C.M. Creager. Radially stiffened shape memory alloy tire. US Patent No. 10427461. 1 October 2019.
- S.C. Kwon, S.H. Jeon, H.U. Oh. Cryogenics. 67, 19 (2015). [Crossref](#)
- W. Huang, S. Pellegrino, D.P. Bashford. Shape memory alloy actuators for deployable structures. In: Proc. Spacecraft Structures. Materials and Mechanical Testing. ESA SP — 386, Noordwijk (1996) p. 53.
- S. Mahdis, C. Youngjae. Acta Biomater. 21, 20 (2015). [Crossref](#)
- J.W. Mwangi, L.T. Nguyen, V.D. Bui, T. Berger, H. Zeidler, A. Schubert. J. Manuf. Process. 38, 355 (2019). [Crossref](#)
- M. Geetha, A.K. Singh, R. Asokamani, A.K. Gogia. Prog. Mater. Sci. 54, 397 (2009). [Crossref](#)
- S. Daly, G. Ravichandran, K. Bhattacharya. Acta Mater. 55, 3593 (2007). [Crossref](#)
- A.L. Gloanec, G. Bilotta, M. Gerland. Mater. Sci. Eng. A. 564 (1), 351 (2013). [Crossref](#)
- A. Misochenko, J.V. Tilak Kumar, S. Jayaprakasam, K.A. Padmanabhan, V. Stolyarov. Defect Diffus. Forum. 385, 169 (2018). [Crossref](#)
- E. Ryklina, K. Polyakova, S. Prokoshkin. Shap. Mem. Superelasticity. 6, 157 (2020). [Crossref](#)
- V.G. Pushin, V.V. Stolyarov, R.Z. Valiev, T.C. Lowe, Y.T. Zhu. Mater. Sci. Eng. A. 410–411, 386 (2005). [Crossref](#)
- A.V. Sergueeva, C. Song, R.Z. Valiev, A.K. Mukherjee. Mater. Sci. Eng. A. 339, 159 (2003). [Crossref](#)
- V. Brailovski, S.D. Prokoshkin, I.Y. Khmelevskaya, K.E. Inaekyan, V. Demers, S.V. Dobatkin, E.V. Tatyatin. Mater. Trans. 47, 795 (2006). [Crossref](#)
- S.D. Prokoshkin, V. Brailovski, K.E. Inaekyan, V. Demers, I.Y. Khmelevskaya, S.V. Dobatkin, E.V. Tatyatin. Mater. Sci. Eng. A. 481–482, 114 (2008). [Crossref](#)
- V. Demers, V. Brailovski, S.D. Prokoshkin, K.E. Inaekyan. Mater. Sci. Eng. A. 513–514, 185 (2009). [Crossref](#)
- V. Brailovski, S.D. Prokoshkin, K. Inaekyana, V. Demers. J. Alloys Compd. 509, 2066 (2011). [Crossref](#)
- E.O. Nasakina, M.A. Sudarchikova, K.V. Sergienko, S.V. Konushkin, M.A. Sevost'yanov. Nanomaterials. 9, 1569 (2019). [Crossref](#)
- S. Nagaraja, S.J. L. Sullivan, P.R. Stafford, A.D. Lucas, E. Malkin. Acta Biomater. 72, 424 (2018). [Crossref](#)
- S.J. L. Sullivan, M.L. Dreher, J. Zheng, L. Chen, D. Madamba, K. Miyashiro, C. Trépanier, S. Nagaraja. Shap. Mem. Superelasticity. 1, 319 (2015). [Crossref](#)
- S. Aksöz. Arab. J. Sci. Eng. 42, 2573 (2017). [Crossref](#)
- X. Li, H. Chen, W. Guo, Y. Guan, Z. Wang, Q. Zeng, X. Wang. Intermetallics. 131, 107114 (2021). [Crossref](#)
- R. Zhu, G. Tang, S. Shi, M. Fu. J. Mater. Process. Technol. 213, 30 (2013). [Crossref](#)
- O. A. Troitskii. JETP Lett. 10, 18 (1969).
- M. J. Kim, S. Yoon, S. Park, H. J. Jeong, J. W. Park, K. Kim, J. Jo, T. Heo, S. T. Hong, S. H. Cho, Y. K. Kwon, I. S. Choi, M. Kim, H. N. Han. Appl. Mater. Today. 21, 100874 (2020). [Crossref](#)
- T.A. Perkins, T.J. Kronenberger, J.T. Roth. Transactions of the ASME. 129, 84 (2007). [Crossref](#)
- S.D. Prokoshkin, V.V. Stolyarov, A.V. Korotitskii, K.E. Inaekyan, E.S. Danilov, I.Y. Khmelevskaya, A.M. Glezer, S.Y. Makushev, U.K. Ugurchiev. Phys. Met. Metallogr. 108, 616 (2009). [Crossref](#)
- J.V. Tilak Kumar, S. Jayaprakasam, K.A. Padmanabhan, A. Misochenko, V. Stolyarov. Mater. Charact. 149, 47 (2019). [Crossref](#)
- R. Zhu, G. Tang. Mater. Sci. Technol. 33, 546 (2017). [Crossref](#)
- A. Monshi, M. Foroughi, M. Monshi. World J. Nano Sci. Eng. 2 (3), 154 (2012). [Crossref](#)
- G.K. Williamson, W.H. Hall. Acta Metall. 1, 22 (1953). [Crossref](#)
- A.K. Zak, W.H. A. Majid, M.E. Abrishami, R. Yousefi. Solid State Sci. 13, 251 (2011). [Crossref](#)
- S.B. Qadri, J.P. Yang, E.F. Skelton, B.R. Ratna. Appl. Phys. Lett. 70, 1020 (1997). [Crossref](#)
- V.M. Anandakumar, M.A. Khadar. Phys. Status Solidi A. 205, 2666 (2008). [Crossref](#)
- B.P. Jacob, S. Thankachan, S. Xavier, E.M. Mohammed. Phys. Scr. 84, 045702 (2011). [Crossref](#)
- S. Dubinskiy, S. Prokoshkin, V. Sheremetyev, A. Konopatsky, A. Korotitskiy, N. Tabachkova, E. Blinova, A. Glezer, V. Brailovski. J. Alloys Compd. 858, 157733 (2021). [Crossref](#)
- S. Prokoshkin, S. Dubinskiy, A. Korotitskiy, A. Konopatsky, V. Sheremetyev, I. Shchetinin, A. Glezer, V. Brailovski. J. Alloys Compd. 779, 667 (2019). [Crossref](#)
- E. Polatidis, M. Šmíd, I. Kuběna, W.N. Hsu, G. Laplanche, H.V. Swygenhoven. Mater. Des. 191, 108622 (2020). [Crossref](#)
- T. Waitz, T. Antretter, F.D. Fischer, N.K. Simhad, H.P. Karnthaler. J. Mech. Phys. Solids. 55, 419 (2007). [Crossref](#)
- K.L. Ng, Q.P. Sun. Mech. Mater. 38, 41 (2006). [Crossref](#)
- Y. Liu, Z. Xie. In: Progress in Smart Materials and Structures (ed by P.L. Reece). Nova Science Publishers (2007) pp. 29–65.
- I. Karaman, H.E. Karaca, H.J. Maier, Z.P. Luo. Metall. Mater. Trans. A. 34A, 2527 (2003). [Crossref](#)
- J.V. Humbeeck. J. Phys. IV France. 01 (C4), 189 (1991). [Crossref](#)